

## Supporting Information

### **Electrochemical transformation reaction of Cu-MnO in aqueous rechargeable zinc-ion batteries for high performance and long cycle life**

*Fekadu Wubatu Fenta<sup>1</sup>, Bizualem Wakuma Olbasa<sup>1</sup>, Meng-Che Tsai<sup>2</sup>, Misganaw Adigo Weret<sup>3</sup>, Tilahun Awoke Zegeye<sup>1</sup>, Chen-Jui Huang<sup>1</sup>, Wei-Hsiang Huang<sup>2</sup>, Tamene Simachew Zeleke<sup>1</sup>, Niguse Aweke Sahalie<sup>1</sup>, Chih-Wen Pao<sup>5</sup>, She-huang Wu<sup>\*2</sup>, Wei-Nien Su<sup>\*2</sup>, Hongjie Dai<sup>\*4</sup>, and Bing Joe Hwang<sup>\*1,2,5</sup>*

*<sup>1</sup>NanoElectrochemistry Laboratory, Department of Chemical Engineering, National Taiwan University of Science and Technology, Taipei 10607, Taiwan*

*<sup>2</sup>NanoElectrochemistry Laboratory, Graduate Institute of Applied Science and Technology, National Taiwan University of Science and Technology, Taipei 10607, Taiwan*

*<sup>3</sup>Department of Materials Science and Engineering, National Taiwan University of Science and Technology, Taipei 10607, Taiwan*

*<sup>4</sup>Department of Chemistry, Stanford University, Stanford, California 94305, United State*

*<sup>5</sup>National Synchrotron Radiation Research Center, Hsin-Chu 30076, Taiwan*

Table S1 XRD fitting of Cu-MnO nanospheres.

<b>d</b>	<b>2 Theta</b>	<b>I Fix</b>	<b>h</b>	<b>k</b>	<b>l</b>
2.56690	34.926	633	1	1	1
2.22300	40.548	1000	2	0	0
1.57190	58.687	489	2	2	0
1.34052	70.147	178	3	1	1
1.28345	73.765	125	2	2	2

a = b = c = 4.44600, Lattice: Cubic, Space group: Fm-3m (225)

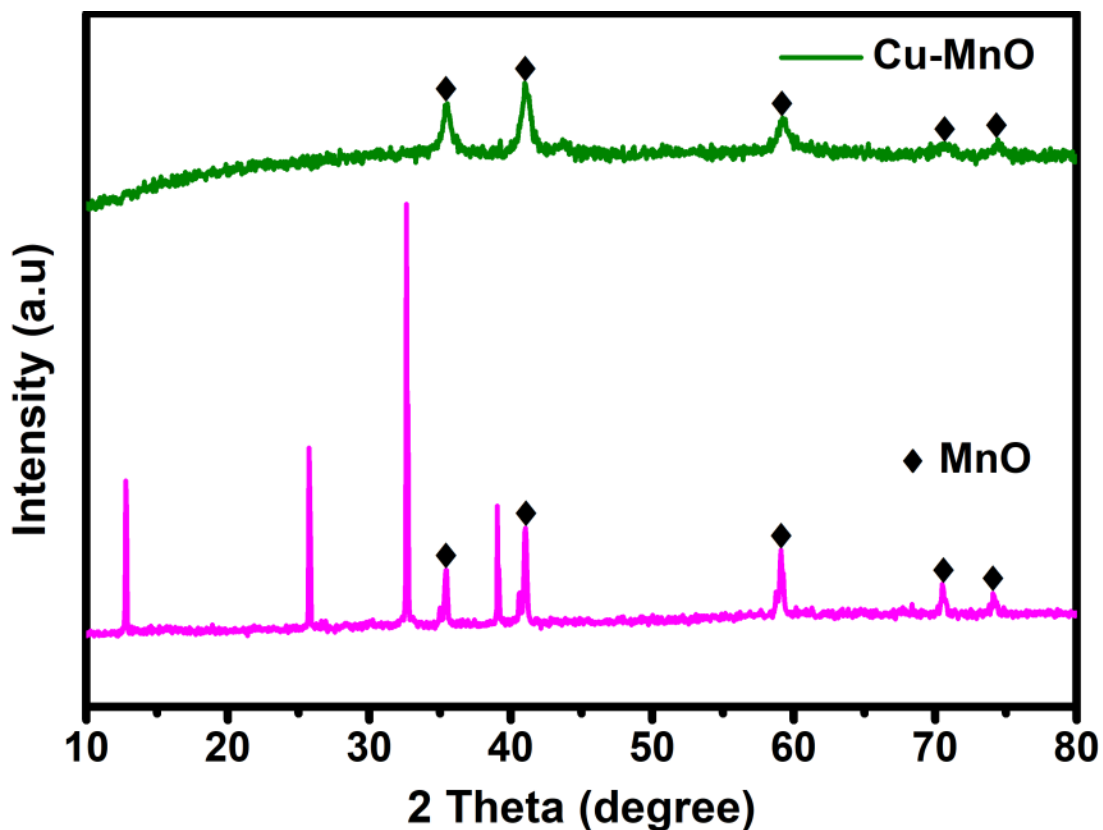


Fig. S1 XRD patterns of MnO synthesized from  $\delta$ -MnO<sub>2</sub> without the presence of tetrakis(acetonitrile)copper(I) hexafluorophosphate ([Cu(CH<sub>3</sub>CN)<sub>4</sub>]PF<sub>6</sub>).

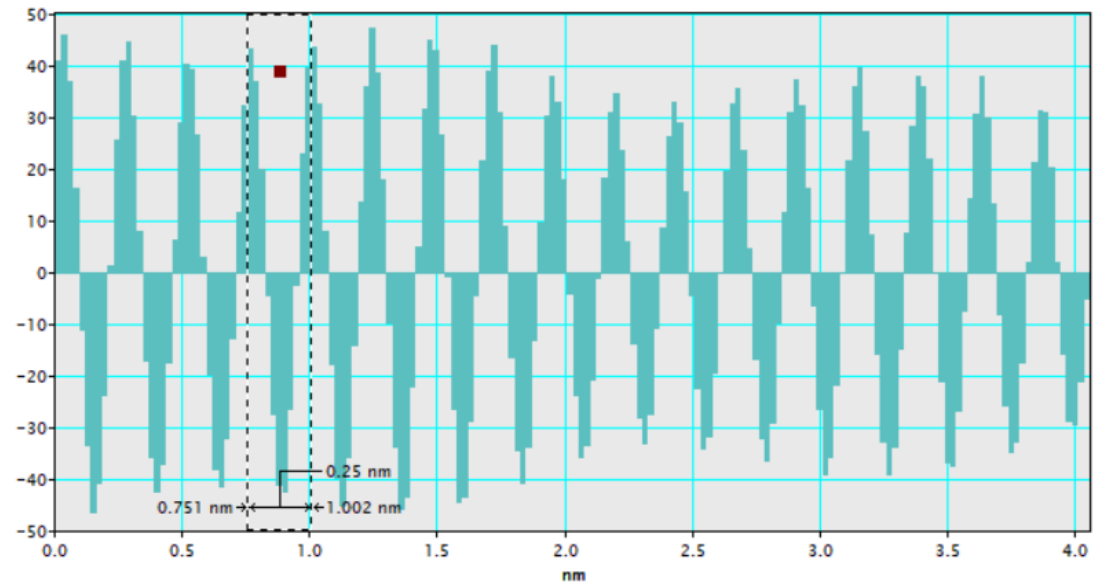


Fig. S2 Determination of crystal lattice spacing in Cu-MnO nanospheres from HRTEM analysis.

Table S2. Linear combination fit (LCF) results of the Cu K-edge XANES spectra of Cu-MnO nanospheres.

Sample	LCF results (%)			LCF parameters	
	Cu	Cu <sub>2</sub> O	CuO	R-factor	Chi-square
Cu-MnO	73.4	26.6	0	$1.1 \times 10^{-3}$	$2.1 \times 10^{-4}$

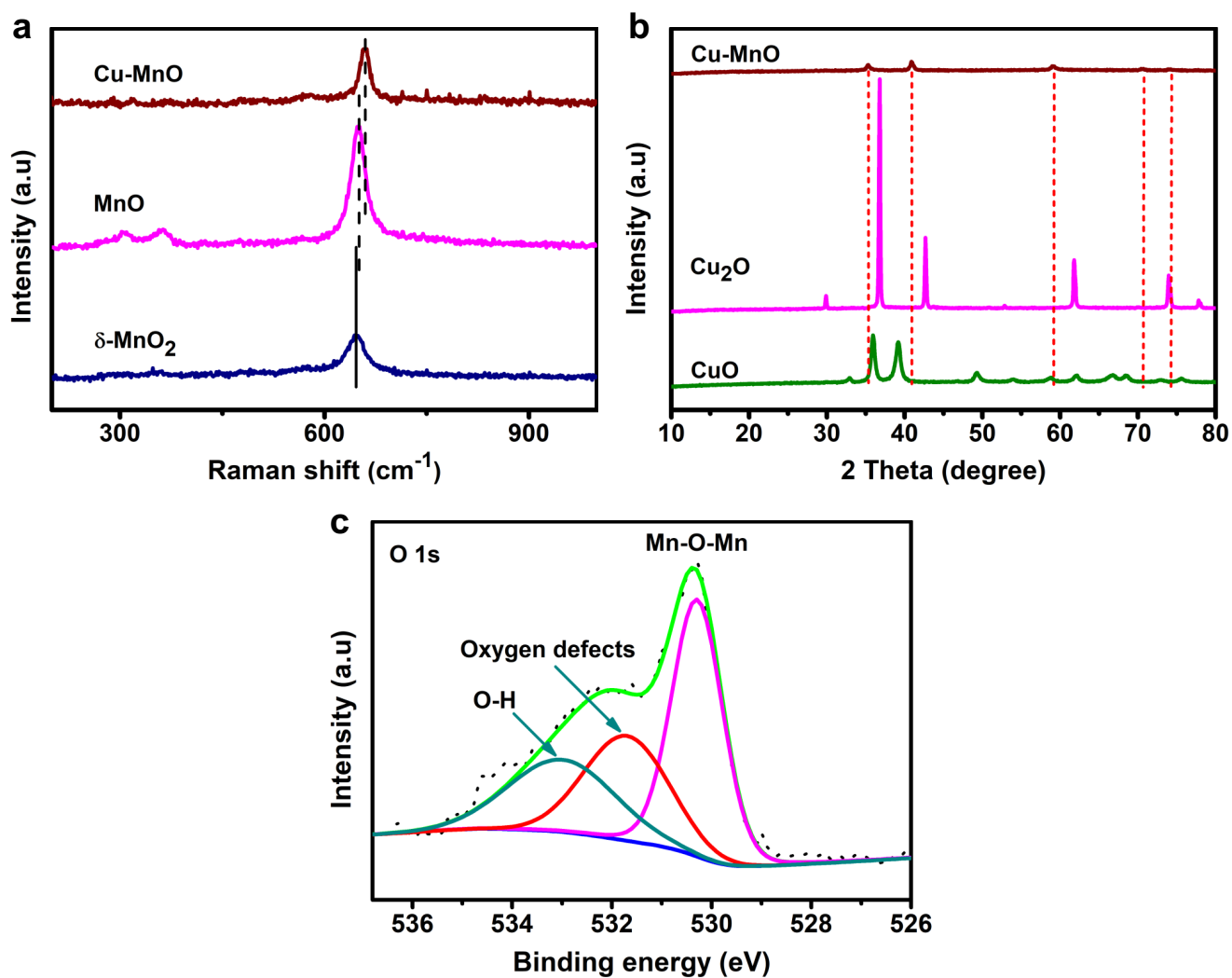


Fig. S3. (a) Raman spectra of commercial MnO and as-synthesized Cu-MnO. (b) XRD patterns of Cu-MnO, Cu<sub>2</sub>O, and CuO, confirming no copper oxides in Cu-MnO. (c) High-resolution O 1s XPS spectra of Cu-MnO.

Table S3. ICP-OES analysis of Cu-MnO nanospheres.

Sample	Cu (mmol/L)	Mn (mmol/L)	Cu/Mn
Cu-MnO	0.0069	0.079	0.09

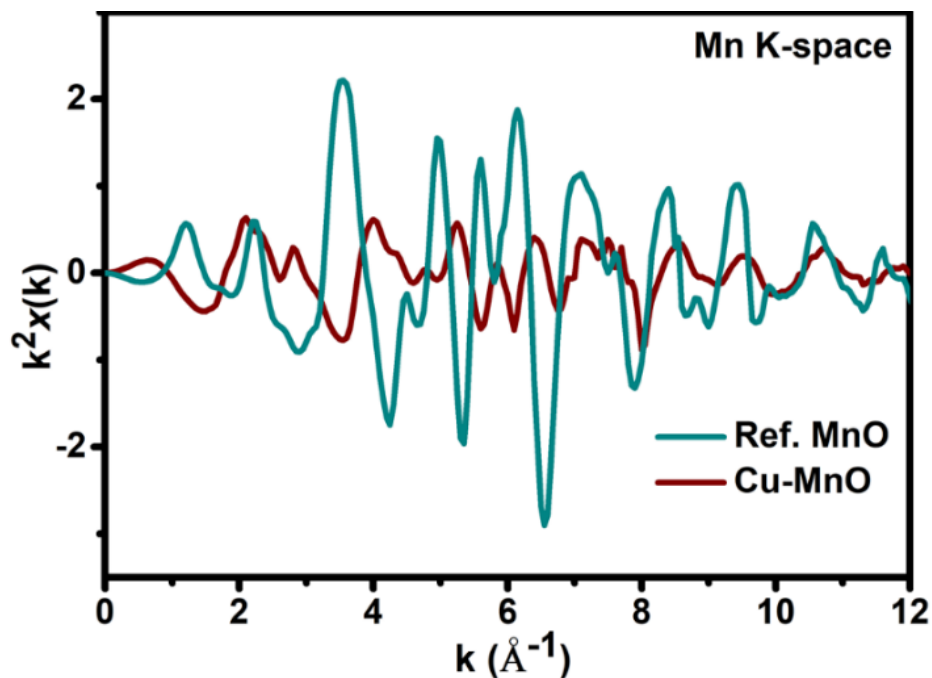


Fig. S4 Mn K-edge extended XANES oscillation functions data for commercial MnO and as-synthesized Cu-MnO nanospheres.

Table S4. Local structure parameters of Cu-MnO around Mn estimated by EXAFS analysis.

Sample	Shell	$N^{[a]}$	$R$ (Å) <sup>[b]</sup>	$\Delta E_0$ (eV) <sup>[c]</sup>	$\sigma^2$ (Å <sup>2</sup> ) <sup>[d]</sup>	R-factor( $\times 10^{-3}$ )
Ref. MnO	Mn-O	$6.0 \pm 1.1$	$2.21 \pm 0.02$	-3.1	0.009	1.2
	Mn-Mn	$12.0 \pm 1.3$	$3.13 \pm 0.01$	-5.5	0.009	
Cu-MnO	Mn-O (short)	$2.0 \pm 1.0$	$1.94 \pm 0.04$	0.9	0.005	7.3
	Mn-O (long)	$2.3 \pm 1.4$	$2.19 \pm 0.05$	-2.9	0.005	
	Mn-Mn (short)	$1.8 \pm 0.8$	$2.87 \pm 0.03$	-6.6	0.008	
	Mn-Mn (long)	$4.1 \pm 0.7$	$3.11 \pm 0.03$	-6.6	0.008	

[a]  $N$  = Coordination number; [b]  $R$  = Distance between absorber and backscatter atoms; [c]  $\Delta E_0$  = energy shift; [d]  $\sigma^2$  = Debye-Waller factor; Fitting K-range = 2.8-11.0

The vacancy of manganese and oxygen in Cu-MnO can be calculated from EXAFS fitting data (table S4) as follows and summarized in Table S4.

$$\text{Manganese Vacancy} = 1 - (N_{\text{Mn-Mn in Cu-MnO}}/N_{\text{Mn-Mn in MnO}}) = 1 - 5.9/12 = 0.51$$

$$\text{Oxygen Vacancy} = 1 - (N_{\text{Mn-O in Cu-MnO}}/N_{\text{Mn-O in MnO}}) = 1 - 4.3/6 = 0.28$$

Table S5. Calculated percentage of manganese vacancy and Oxygen vacancy in Cu-MnO nanospheres.

<b>Sample</b>	<b>Manganese vacancy</b>	<b>Oxygen vacancy</b>
Cu-MnO	51%	28%

Table S6. ICP-OES analysis of Cu-MnO electrode at 5<sup>th</sup> cycle fully charged state.

<b>Sample</b>	<b>Cu (mmol/L)</b>	<b>Mn (mmol/L)</b>	<b>Zn (mmol/L)</b>	<b>Zn/Mn (mmol/L)</b>	<b>Cu/Mn</b>
Cu-MnO electrode	0.00172	0.160974	0.047854	0.3	0.01

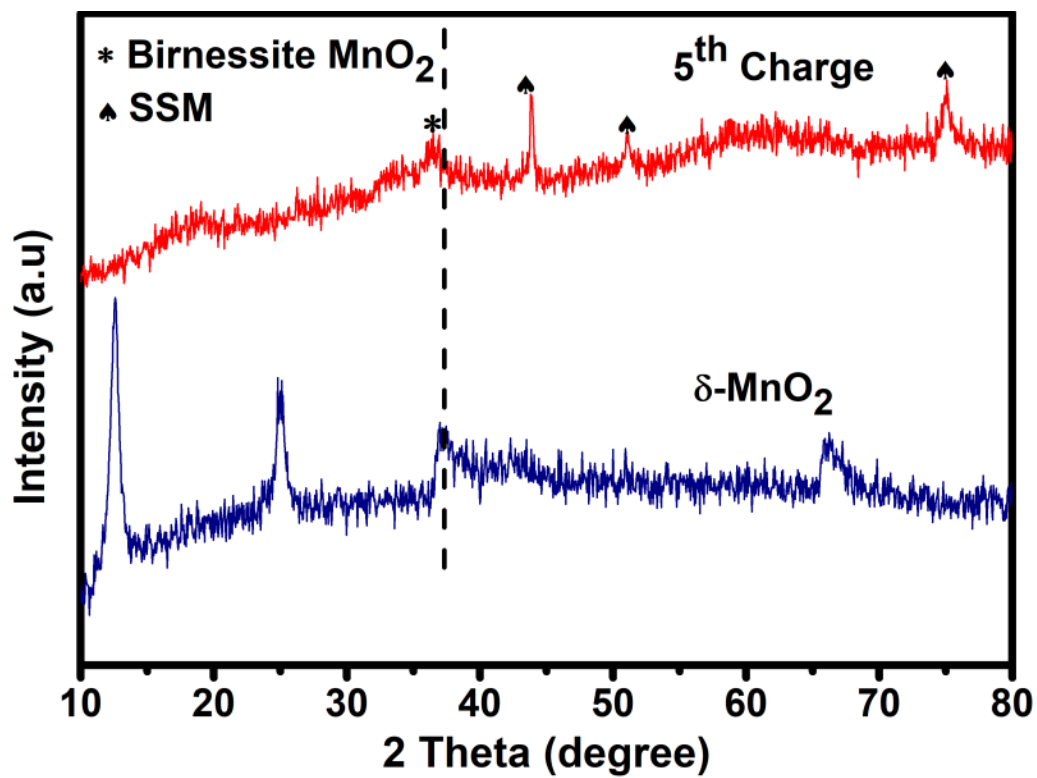


Fig. S6 Comparison between  $\delta$ -MnO<sub>2</sub> prepared by hydrothermal method and Cu-MnO electrode at 5<sup>th</sup> cycle, lower angle shifts in fully charged Cu-MnO indicating the interlayer expansion due to zinc ion and structural water intercalation. SSM, stainless steel mesh.

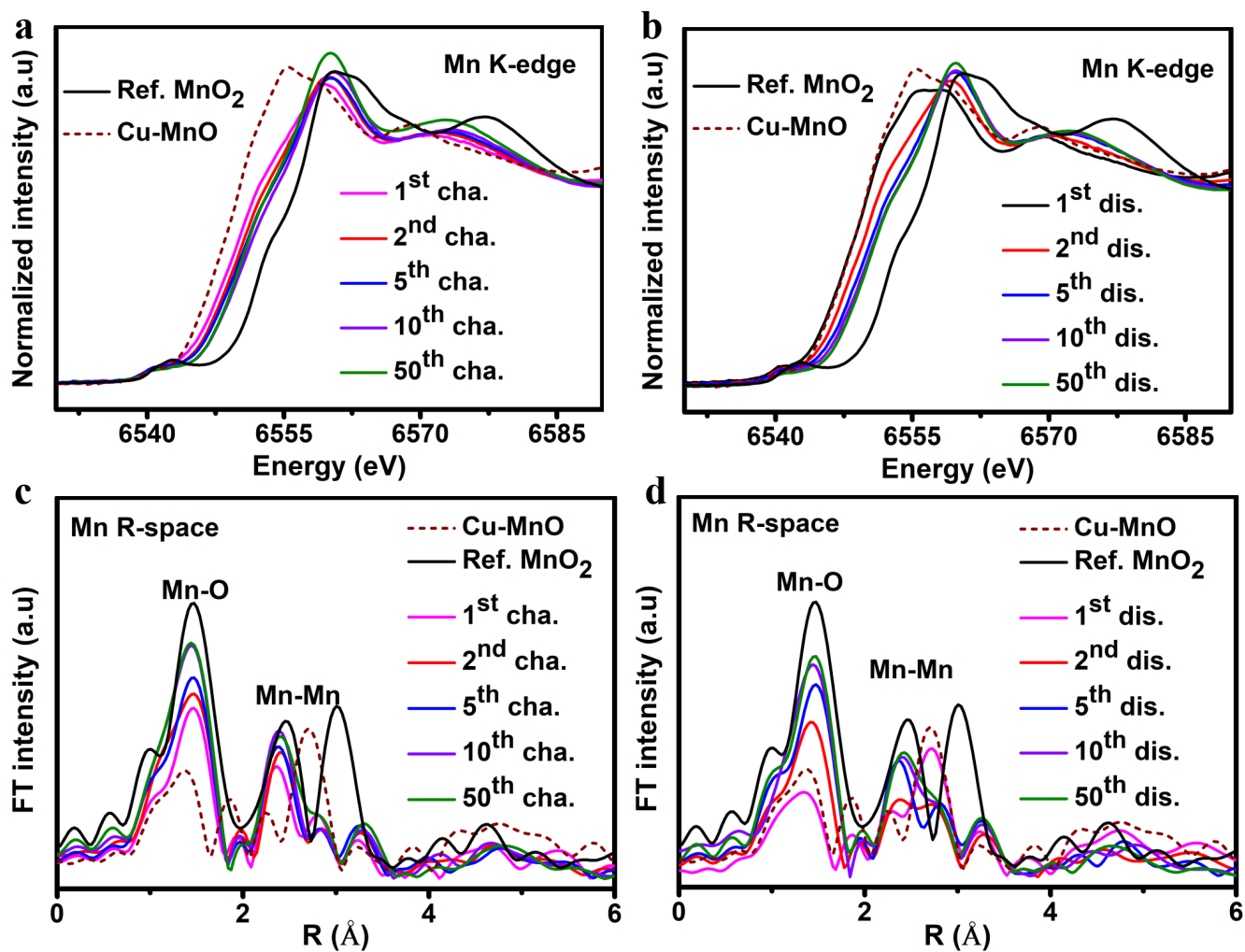


Fig. S7 Mn K-edge XANES spectra of Cu-MnO and its (a) charge; (b) discharge electrodes at the 1<sup>st</sup>, 2<sup>nd</sup>, 5<sup>th</sup>, 10<sup>th</sup>, and 50<sup>th</sup> cycles. The corresponding Fourier transform of Mn K-edge EXAFS spectra during (c) charge; (d) discharge at the 1<sup>st</sup>, 2<sup>nd</sup>, 5<sup>th</sup>, 10<sup>th</sup>, and 50<sup>th</sup> cycles.

Table S7. Analysis of the fully charged and discharged Cu-MnO electrodes local structure parameters around Mn estimated by EXAFS

Sample	shell	N <sup>[a]</sup>	R (Å) <sup>[b]</sup>	$\Delta E_0$ (eV) <sup>[c]</sup>	$\sigma^2$ (Å <sup>2</sup> ) <sup>[d]</sup>	R-factor ( $\times 10^{-3}$ )
Cu-MnO	Mn-O (short)	2.0 $\pm$ 1.0	1.94 $\pm$ 0.04	0.9	0.005	7.3
	Mn-Mn (long)	2.3 $\pm$ 1.4	2.19 $\pm$ 0.05	-2.9	0.005	
	Mn-Mn (short)	1.8 $\pm$ 0.8	2.87 $\pm$ 0.03	-6.6	0.008	
	Mn-Mn (long)	4.1 $\pm$ 0.7	3.11 $\pm$ 0.03	-6.6	0.008	
Full discharge	Mn-O	4.8 $\pm$ 0.2	1.92 $\pm$ 0.01	-1.9	0.002	3.1
	Mn-Mn (short)	2.5 $\pm$ 0.5	2.90 $\pm$ 0.05	-1.8	0.008	
	Mn-Mn (long)	2.3 $\pm$ 0.5	3.08 $\pm$ 0.04	-1.8	0.008	
Full charge	Mn-O	5.8 $\pm$ 1.0	1.91 $\pm$ 0.02	-0.9	0.004	2.4
	Mn-Mn (short)	2.9 $\pm$ 1.0	2.89 $\pm$ 0.06	-1.2	0.008	
	Mn-Mn (long)	2.1 $\pm$ 1.7	3.08 $\pm$ 0.08	-1.2	0.008	

[a]  $N$  = Coordination number; [b]  $R$  = Distance between absorber and backscatter atoms; [c]  $\Delta E_0$  = Energy shift; [d]  $\sigma^2$  = Debye-Waller factor; Fitting K-range = 2.8-11.8

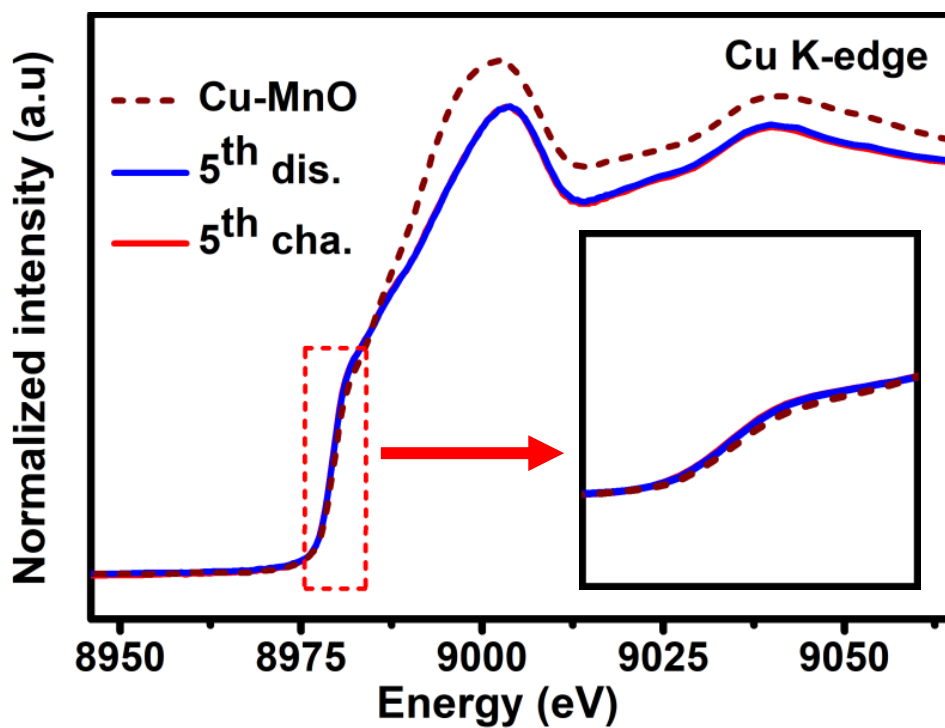


Fig. S8 Normalized Cu K-edge XANES spectra of Cu-MnO and its charged and discharged electrodes at the 5<sup>th</sup> cycle.

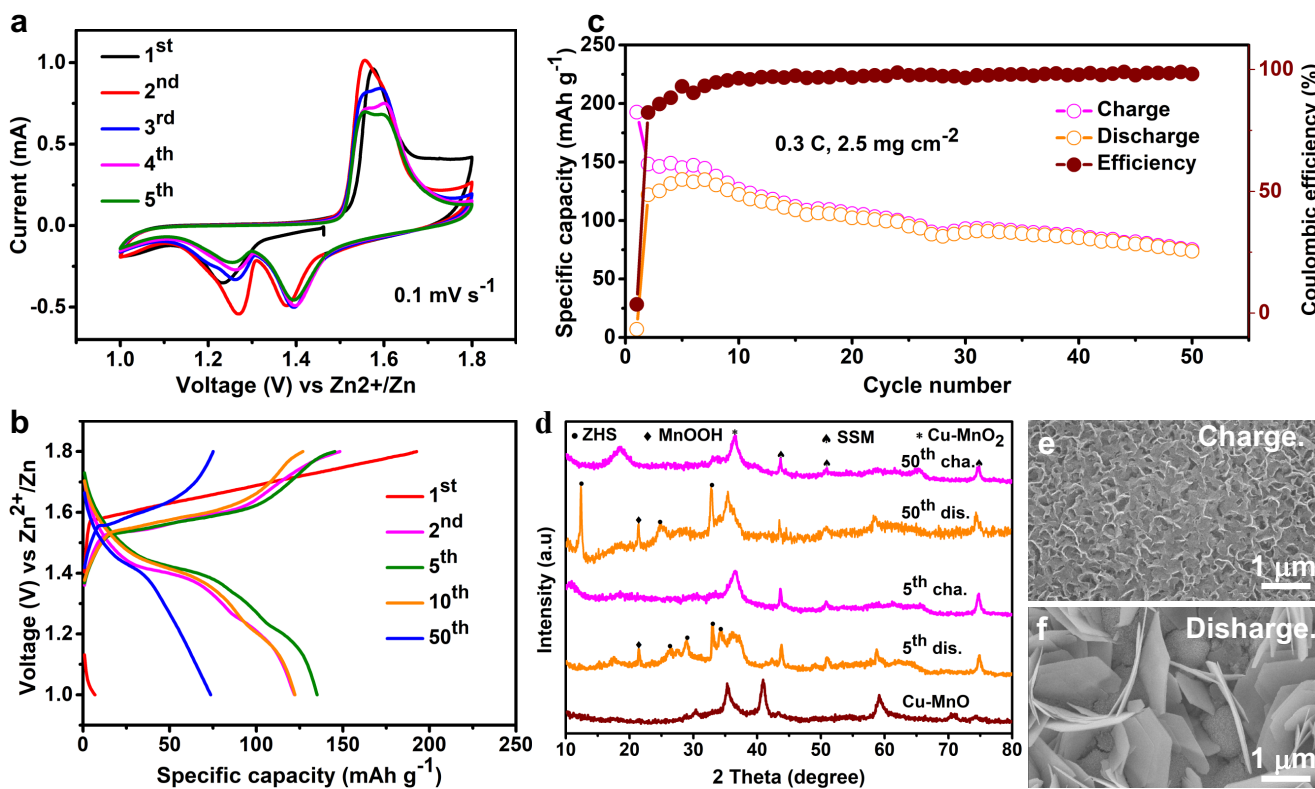


Fig. S9 Electrochemical performance and mechanism of Zn/Cu-MnO batteries in 2 M ZnSO<sub>4</sub> electrolyte in the voltage range of 1-1.8 V vs Zn<sup>2+</sup>/Zn. (a) CV curves at a scan rate of 0.1 mV s<sup>-1</sup>. (b) Charge/discharge profiles at 0.3 C. (c) Cycling performance. (d) Ex-situ XRD patterns after the 5<sup>th</sup> cycle at 0.3 C. The SEM images at fully (e) charged and (f) discharged states of 5<sup>th</sup> cycle.

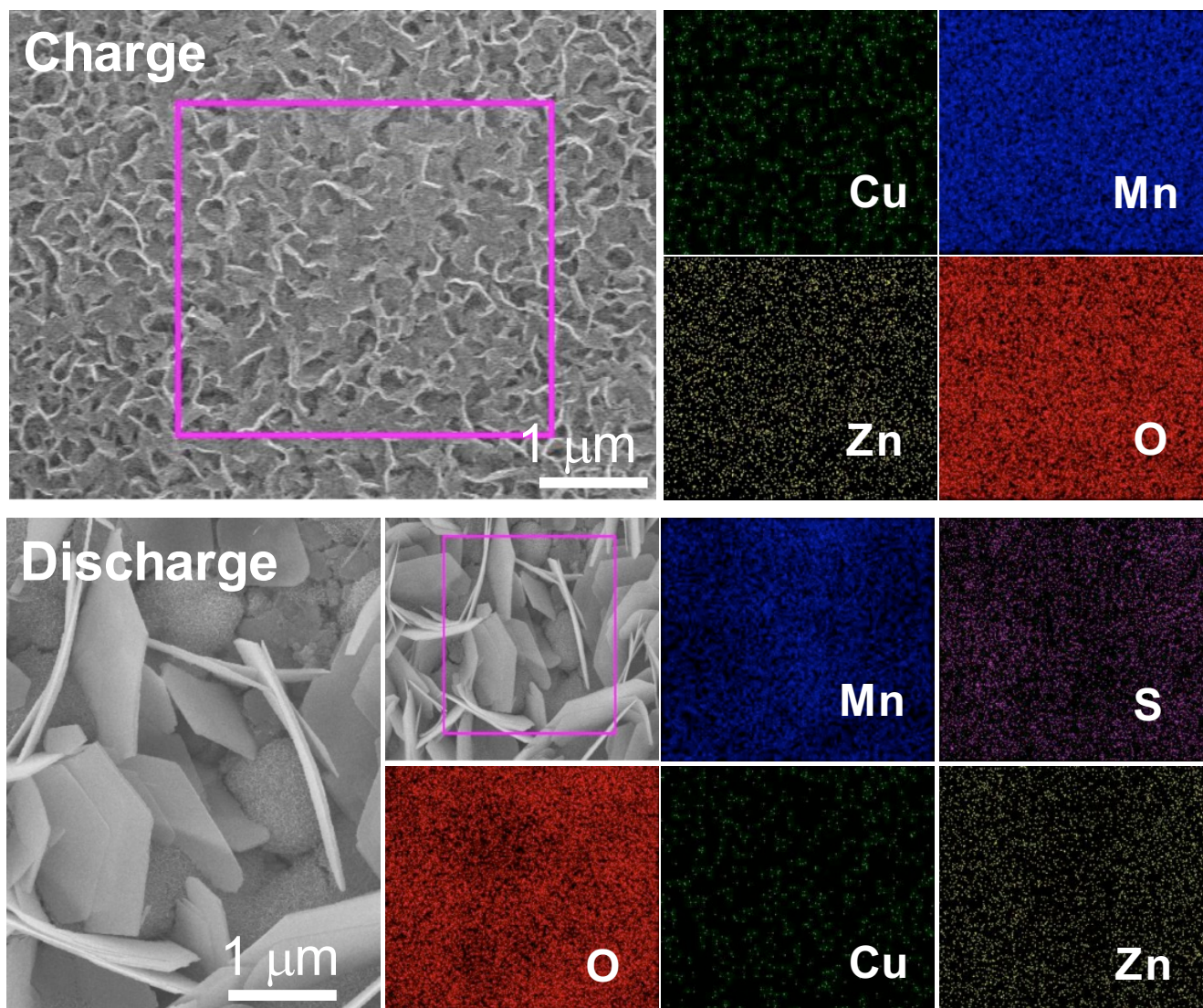


Fig. S10 SEM images and corresponding EDS elemental mapping images of Cu-MnO electrodes showing the distribution of elements after the 5<sup>th</sup> cycle at (a) charged and (b) discharged states in ZnSO<sub>4</sub> electrolyte.

The electrochemical performance of Cu-MnO nanospheres was analyzed in coin cells using ZnSO<sub>4</sub> electrolyte within the potential window 1.0-1.8 V vs Zn<sup>2+</sup>/Zn. As shown in Fig. S9(a), the initial CV curves show one reduction/oxidation peaks at 1.22/1.57 V. In the subsequent cycles, there are two pairs of reduction/oxidation peaks at 1.26/1.39 and 1.56/1.6 V. They can be attributed to the H<sup>+</sup>/Zn<sup>2+</sup> co-insertion/extraction processes.<sup>1</sup> Furthermore, the CV curves after the first cycle show similar shape, indicating the reversibility of the reduction/oxidation process of Zn/Cu-MnO batteries in ZnSO<sub>4</sub> electrolyte. In addition, Zn/Cu-MnO battery provides low initial discharge and high charge capacities of 6.8 and 192.6 mAh g<sup>-1</sup>, respectively (Fig.S9(b)). The redox peaks in a CV and charge-discharge curves are consistent with each other. However, The voltage (Fig. S9(a)) and charge-discharge profiles (Fig. S9(b)) in the first cycle are different from those of the subsequent cycles, suggesting irreversible phenomena in the first cycle. These data are consistent with the electrochemical behavior of Zn/Cu-MnO batteries with MnSO<sub>4</sub> additive in ZnSO<sub>4</sub> electrolyte as shown in Fig. 3a-b. Therefore, the voltage profiles and the charge-discharge curves of Zn/Cu-MnO batteries in aqueous electrolytes, with and without MnSO<sub>4</sub>, showing similar behavior that suggests MnSO<sub>4</sub> additive do not affect the redox reactions in Cu-MnO electrodes. The redox peaks are consistent with the plateaux in the charge-discharge profiles with and without MnSO<sub>4</sub> additive in ZnSO<sub>4</sub> electrolytes. However, Compared with the cyclic stability in MnSO<sub>4</sub> additive (Fig. 6e), Zn/Cu-MnO battery in ZnSO<sub>4</sub> electrolyte show rapid deterioration in capacity as shown in Fig. S9(c). This result suggests the gradual increment of the capacity in MnSO<sub>4</sub> additive could be associated with the oxidation of Mn<sup>2+</sup> from electrolyte and structural transformation.

Moreover, to elucidate the phase transformation and energy storage mechanism of Cu-MnO electrodes during charge-discharge without Mn<sup>2+</sup> additive, we further investigate the structural and morphological change of Cu-MnO electrodes using ex-situ XRD and SEM. The Cu-MnO peaks disappeared and there is a new, broad, and reversible peak at  $2\theta = 36.6^\circ$ , which indicates the transformation of Cu-MnO to layered birnessite (Cu-MnO<sub>2</sub>.nH<sub>2</sub>O) (Fig. S9(d)). Moreover, several new XRD peaks appear during discharge,

which can be associated with zinc hydroxide sulfate hydrate  $((\text{Zn}(\text{OH})_2)_3(\text{ZnSO}_4) \cdot x\text{H}_2\text{O})$ , ZHS) precipitate and  $\text{MnOOH}$  conversion product. The structural evolution, when charged to 1.8 V, follows the opposite trend to that of discharge to 1.0 V. The SEM image (Fig. S9(e-f)) shows ZHS precipitate appears and disappears on the fully discharged and charged electrode surface, respectively. The SEM-EDS (Fig. S10) elemental mapping further supports the result of ex-situ XRD and SEM analyses. Overall, the structural transformation and energy storage mechanism of Zn/Cu-MnO batteries with and without  $\text{MnSO}_4$  additive in  $\text{ZnSO}_4$  electrolytes are identical. However, the performance of Cu-MnO electrodes significantly improved with  $\text{MnSO}_4$  additive in  $\text{ZnSO}_4$  electrolyte, which is consistent with the literature.<sup>2</sup>

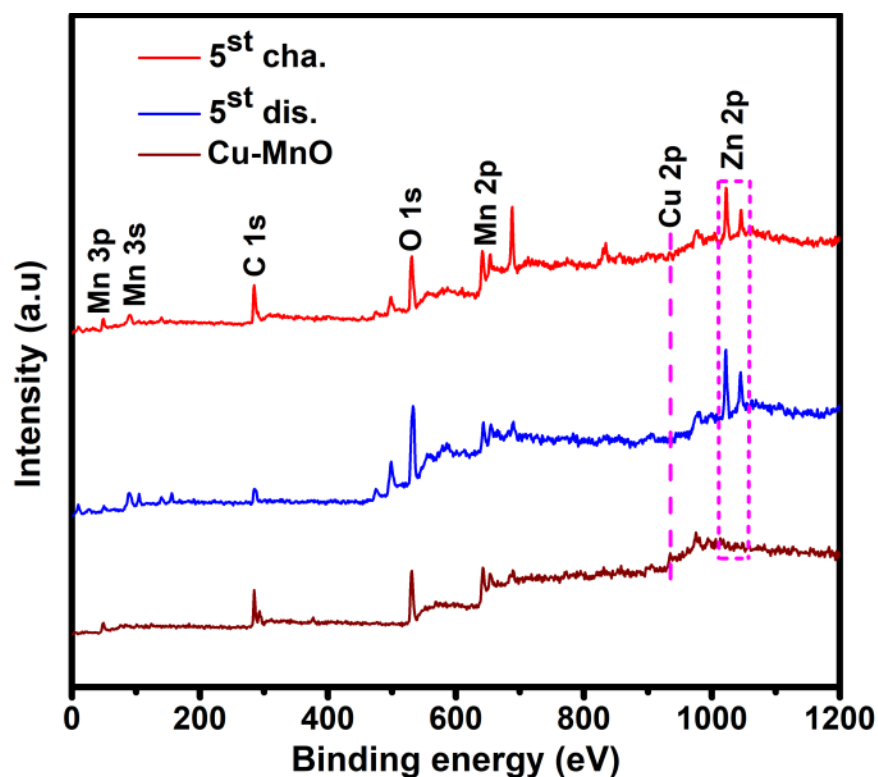


Fig. S11 XPS survey spectra of Cu-MnO and its fully discharged and charged states.

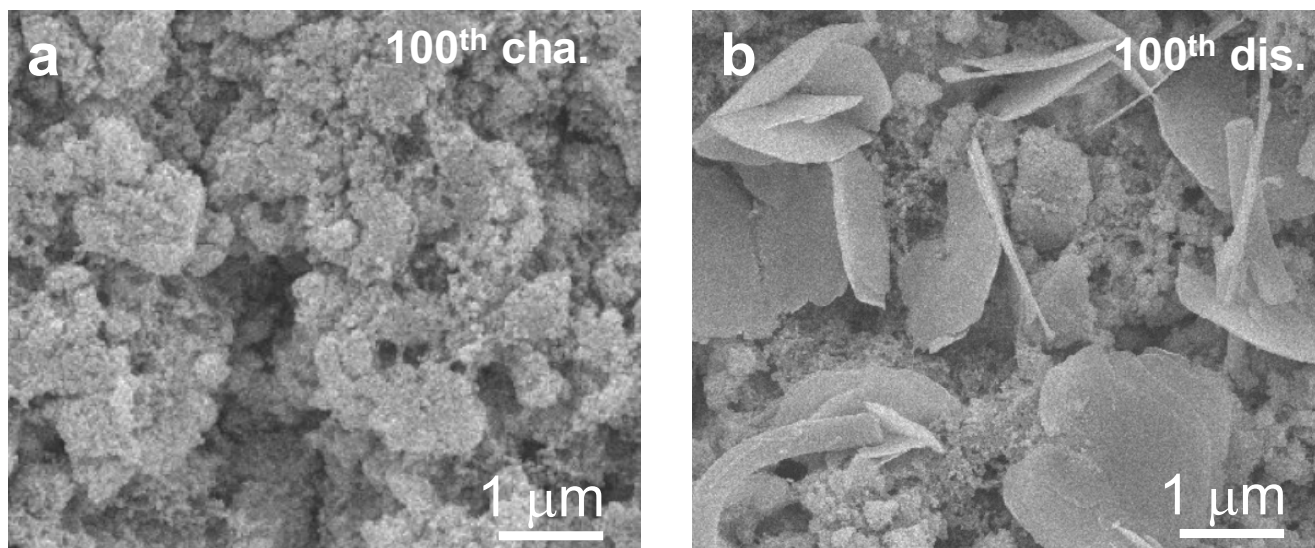


Fig. S12 SEM images of Cu-MnO electrodes at fully (a) charged and (b) discharged states after 100<sup>th</sup> cycles.

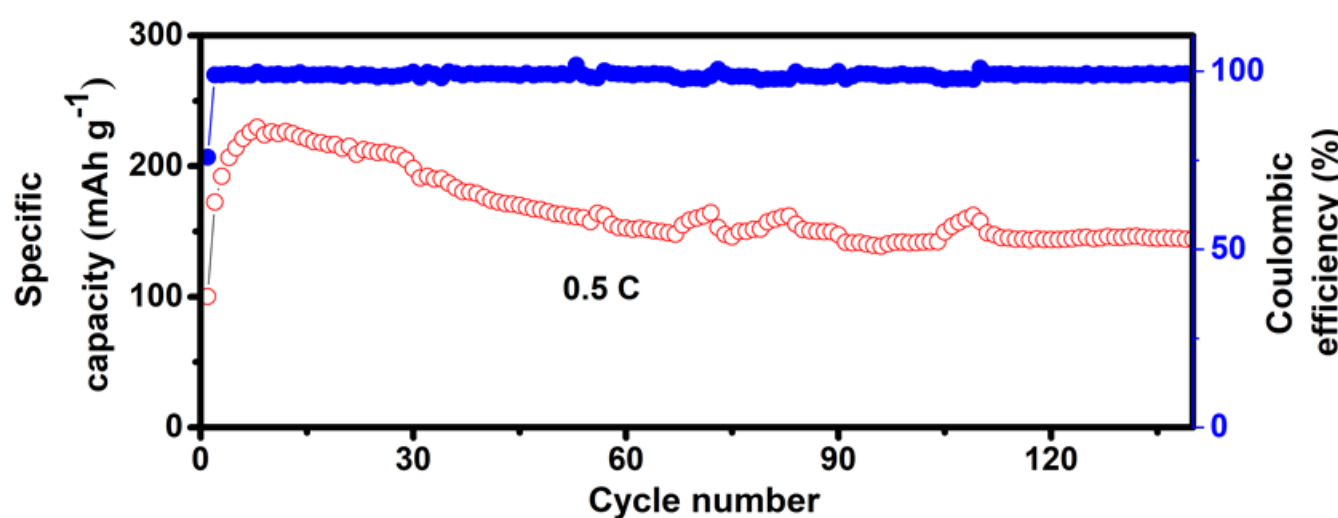


Fig. S13 Cycling performance of Zn/ $\delta$ -MnO<sub>2</sub> battery at 0.5 C using 2 M ZnSO<sub>4</sub> and 0.1 M MnSO<sub>4</sub> aqueous electrolyte.

Table S8 Comparison of current density, maximum capacity, and cycle life of different cathode materials in aqueous electrolytes.

<b>Cathode materials</b>	<b>Electrolytes</b>	<b>Current density (mA g<sup>-1</sup>)</b>	<b>Maximum capacity (mAh g<sup>-1</sup>)</b>	<b>Cycle number</b>	<b>reference</b>
$\alpha$ -Mn <sub>2</sub> O <sub>3</sub>	2 M ZnSO <sub>4</sub>	100	148	30	3
Mn <sub>3</sub> O <sub>4</sub>	2 M ZnSO <sub>4</sub> + 0.1M MnSO <sub>4</sub>	100	296	50	4
ZnMn <sub>2</sub> O <sub>4</sub>	3 M Zn(CF <sub>3</sub> SO <sub>3</sub> ) <sub>2</sub>	50	150	50	5
$\beta$ -MnO <sub>2</sub>	3 M Zn(CF <sub>3</sub> SO <sub>3</sub> ) <sub>2</sub> + 0.1 M Mn(CF <sub>3</sub> SO <sub>3</sub> )	200	150	225	6
$\alpha$ -MnO <sub>2</sub>	0.1 M Zn(NO <sub>3</sub> )	150	130	100	7
$\delta$ -MnO <sub>2</sub>	1 M ZnSO <sub>4</sub>	83	150	100	8
Cu-MnO	2 M ZnSO <sub>4</sub> + 0.1M MnSO <sub>4</sub>	154	320	210	This work

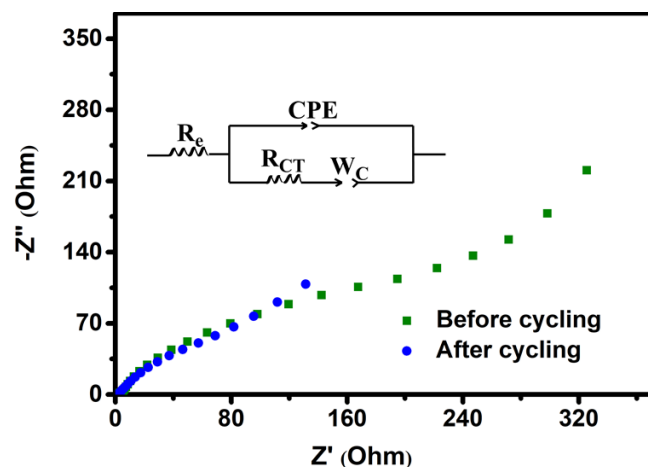


Fig. S14 EIS analysis for pristine Cu-MnO and after 10<sup>th</sup> cycle.

Table S9 Parameters obtained from fitted EIS plots with equivalent circuit.

Sample	Resistance ( $\Omega$ )	
	$R_e$	$R_{ct}$
Before cycling	1.945	223.05
After cycling	0.754	58.97

## References

1. J. Huang, Z. Wang, M. Hou, X. Dong, Y. Liu, Y. Wang and Y. Xia, *Nat. commun.*, 2018, **9**, 1-8.
2. Y. Huang, J. Mou, W. Liu, X. Wang, L. Dong, F. Kang and C. Xu, *Nano-Micro Lett.*, 2019, **11**, 49.
3. B. Jiang, C. Xu, C. Wu, L. Dong, J. Li and F. Kang, *Electrochim. Acta*, 2017, **229**, 422-428.
4. C. Zhu, G. Fang, J. Zhou, J. Guo, Z. Wang, C. Wang, J. Li, Y. Tang and S. Liang, *J. Mater. Chem. A*, 2018, **6**, 9677-9683.
5. N. Zhang, F. Cheng, Y. Liu, Q. Zhao, K. Lei, C. Chen, X. Liu and J. Chen, *J. Am. Chem. Soc.*, 2016, **138**, 12894-12901.
6. N. Zhang, F. Cheng, J. Liu, L. Wang, X. Long, X. Liu, F. Li and J. Chen, *Nat. commun.*, 2017, **8**, 1-9.
7. C. Xu, B. Li, H. Du and F. Kang, *Angew. Chem., Int. Ed.*, 2012, **51**, 933-935.
8. M. H. Alfaruqi, J. Gim, S. Kim, J. Song, D. T. Pham, J. Jo, Z. Xiu, V. Mathew and J. Kim, *Electrochem. Commun.*, 2015, **60**, 121-125.

